A Numerical Study of Traveling Microbursts

LEIGH G. ORF AND JOHN R. ANDERSON

Space Science and Engineering Center, University of Wisconsin—Madison, Madison, Wisconsin

(Manuscript received 29 July 1997, in final form 19 June 1998)

ABSTRACT

An analysis of traveling microbursts in unidirectionally sheared environments is undertaken using a three-dimensional numerical model with 50-m resolution in a 19 × 12 × 4 km domain. For each run, the cooling source is centered at a height of 2 km and travels in an eastward direction of C_m, where C_m = 3, 6, 9, 12, and 15 m s^{-1}. Environmental winds above 2 km are equal to C_m and decay linearly to 0 m s^{-1} below 2 km. The authors examine the kinetic energy budget of each run, focusing on the dynamic features that are not found in a static microburst simulation. As the source speed C_m increases from 0 to 9 m s^{-1}, the magnitude of the surface horizontal winds increase in the direction of source movement. An examination of the dynamic pressure equation shows that rotationally induced pressure work forces are primarily responsible for increasing surface horizontal winds for the moving-source microbursts. In a similar form to previous studies of vertical perturbations in a sheared environment, elevated horizontal vorticity is generated by tilting of environmental vorticity and is strengthened by stretching imposed by the downdraft. The authors' results suggest that the magnitude of the damaging surface winds of a microburst can be enhanced significantly when the parent cloud is moving in a unidirectionally sheared environment.

1. Introduction

Microbursts are short-lived intense downdrafts that are forced by thermodynamic cooling and hydrometeor frictional drag produced by cumulonimbus clouds. Microbursts can cause tornado-strength damage on the ground and are especially dangerous to aircraft in the takeoff and landing phases of flight due to the combination of performance-decreasing downward winds and low-level horizontal shear. For these reasons, microbursts have been the subject of much observational and numerical study since they were categorized by Ted Fujita in 1975. Field studies such as Joint Airport Weather Studies (JAWS) (McCarthy et al. 1982), Northern Illinois Meteorological Research on Downbursts (NIMROD) (Fujita 1979), and Federal Aviation Administration (FAA)–Lincoln Laboratory Operational Weather Studies (FLOWS) (Wolfson et al. 1985) sampled hundreds of microbursts with single Doppler radar and in many cases multi-Doppler radar data of the entire microburst-producing storm (e.g., Lee et al. 1992a; Hjelmfelt 1988; Lin and Hughes 1987; Lin and Coover 1988; Wakimoto et al. 1994; Knupp 1996).

Field studies have shed light on many of the properties of microbursts and have spurred the development of numerical models to simulate microbursts and microburst-producing storms. The types of models used to study microbursts have generally fallen into two categories: subcloud microburst models, in which some sort of forcing, usually microphysical, is imposed in an elevated region of the domain (e.g., Teske and Lewellen 1977; Srivastava 1985; Proctor 1988; Proctor 1989; Anderson et al. 1992; Straka et al. 1993; Orf et al. 1996); and full cloud models, in which the life cycle of a microburst-producing storm is modeled (e.g., Tuttle et al. 1989; Knupp 1989; Hjelmfelt et al. 1989; Straka and Anderson 1993; Parsons and Weisman 1993; Proctor and Bowles 1992). Simulations of microbursts are not limited to computer models; Alahyari and Longmire (1995) simulated microbursts in a laboratory tank by releasing a dense volume of fluid into a less dense ambient fluid and measuring the fluid dynamics using particle image velocimetry.

Fujita (1985) coined the terms ''wet'' and ''dry'' microbursts, where a dry microburst is characterized by less than 0.01 inches of precipitation measured at the ground below the microburst downdraft. Dry microbursts typically occur where the microburst parent cloud is in an environment with a dry boundary layer and a deep dry adiabatic profile that extends to ~3 km AGL or higher. Such environmental conditions are typical in the High Plains of the western United States, and microburst-producing High Plains cumulonimbi often produce dry microbursts primarily forced by the evaporation of rainwater (Wakimoto 1985). Proctor (1988) used

Corresponding author address: Dr. Leigh Orf, Space Science and Engineering Center, University of Wisconsin—Madison, 1225 W. Dayton St., Madison, WI 53706.
E-mail: orf@ssec.wisc.edu

an axisymmetric model with ice-phase microphysics to simulate microburst formation by allowing hydrometeors to fall through the top of the model domain. He found that thermodynamic processes such as the evaporation of rain and the melting of frozen hydrometeors provide much of the negative buoyancy that forces downdraft formation in High Plains dry microbursts. Microbursts that occur in environments with moderately stable, moist boundary layers are usually accompanied by heavy rain at the surface. Proctor (1989) conducted many modeling experiments that explored microburst sensitivity to environment and the type/amount of precipitation, and found that, in general, microbursts occurring in this type of environment were forced primarily by mass loading and occurred when the precipitation shaft exceeded several kilometers in diameter.

Full cloud models and subcloud models have both been used successfully to aid in the understanding of microburst phenomena. Cloud models with detailed microphysics are useful in following the full life cycle of a microburst-producing cumulonimbus cloud and have been used to illustrate the physical and thermodynamical mechanisms behind microburst initiation, as well as the effect of the environment on microburst formation. These cloud modeling studies and observations of microburst-producing storms have shown that microbursts generally favor certain environments over others and that the mechanisms behind microburst formation can be quite different in different environments. Subcloud models are typically run at higher resolution than cloud models and rely on some sort of a priori forcing to initialize the microburst. Subcloud models are generally used to study the detailed structure of the microburst itself rather than the entire microburst-producing storm, and these models typically have not included environmental shear.

In this study, we numerically examine the dynamics of traveling microbursts in unidirectionally sheared environments, where a traveling microburst is defined by Fujita (1985) as a microburst spawned by a moving parent cloud. Observations of microburst-producing storms illustrate that shear not only plays a key role in the development of microburst-producing storms but can also can affect the morphology of the microburst itself. Unidirectional vertical wind shear in the lower few kilometers of the atmosphere can distort the surface outflow, leading to an asymmetric, highly divergent outflow pattern with very strong winds in the direction of storm motion (Fujita 1985). Hjelmfelt (1988) observed a microburst-producing storm that traveled at 8 m s^{-1} and occurred over a weak surface flow. The observed surface outflow pattern was one in which the horizontal winds were strongest in the general direction of storm motion and very weak in the direction opposite of storm motion (see his Fig. 5). A microburst produced from a moving cloud in a sheared environment can also serve as a mechanism for the development of elevated horizontal vorticity. This phenomenon was observed in a case study done by Lee et al. (1992b) of one of the JAWS microbursts where a storm in a nearly unidirectional vertically sheared environment developed a bow-echo radar signature and produced a strong microburst. In this case, the morphology of the storm and the generation of horizontal vorticity was closely connected to the environmental shear profile.

Because our subcloud model is dry, a parameterized forcing function is used to produce the microburst downdraft. The fact that our model contains no microphysics and has a vertical domain of 4 km limits the range of realistic simulations to nonsupercell High Plains–type traveling microbursts where the updraft of the parent cloud is decoupled from the downdraft or is assumed to have collapsed to form the downdraft. Because the forcing (described below) is designed only to represent thermodynamic cooling processes, our simulations exclude the effect of precipitation loading. The lack of microphysics also excludes the effects of hydrometeor advection, which would produce a more realistic cooling forcing especially in the case of the faster moving source runs where there is more environmental shear. By limiting our scope to a particular class of microburst in an idealized environment, we are able to focus on the detailed dynamics of traveling microbursts without the added complexity and computational demands of a model that includes microphysical processes. However, when interpreting modeling results it must be remembered that this modeling study is not intended to be a rigorous, inclusive study of microbursts produced by moving clouds, but a dynamical study of the effects of source movement and unidirectional environmental shear on traveling microburst morphology.

2. Model description

The model used in this study is identical to that described in Orf et al. (1996) with the exception that the first-order constant eddy viscosity turbulence closure has been replaced with a two-equation prognostic k–ϵ model. The model is a dry, nonhydrostatic quasi-compressible subcloud model run on an isotropic grid with 50-m resolution with a computational domain of 19 $\times$ 6 $\times$ 4 km, with mirror symmetry about the x axis. The subcloud environment is neutral below 3 km and slightly stable above. The model equation system is as follows:

$$\frac{\partial U_i}{\partial t} = -\mathbf{U}\cdot\nabla U_i - \frac{1}{\overline{\rho}}\nabla_i p + \delta_{i3} g\frac{\theta}{\overline{\theta}} + \frac{\partial}{\partial x_j}\left[\nu\left(\frac{\partial U_i}{\partial x_j} + \frac{\partial U_j}{\partial x_i}\right)\right] \quad (1)$$

$$\frac{\partial \theta}{\partial t} = -\mathbf{U}\cdot\nabla\theta + Q(x, y, z, t) + \frac{\partial}{\partial x_i}\left(\alpha_K \nu \frac{\partial \theta}{\partial x_i}\right) \quad (2)$$

$$\frac{\partial p}{\partial t} = -c_s^2\left(\overline{\rho}\frac{\partial u}{\partial x} + \overline{\rho}\frac{\partial v}{\partial y} + \frac{\partial(\overline{\rho}w)}{\partial z}\right) + \frac{\partial}{\partial x_i}\left(\alpha_K \nu \frac{\partial p}{\partial x_i}\right) \quad (3)$$

$$\frac{\partial \overline{k}}{\partial t} = -\mathbf{U}\cdot\boldsymbol{\nabla}\overline{k} - \overline{\epsilon} - \overline{\tau}_{ij}S_{ij} + \frac{\nu_T}{\overline{\theta}}\frac{\partial(\overline{\theta}+\theta)}{\partial x_i}\frac{\partial(\overline{p}+p)}{\partial x_i} + \frac{\partial}{\partial x_i}\left(\alpha_K \nu \frac{\partial \overline{k}}{\partial x_i}\right) \quad (4)$$

$$\frac{\partial \overline{\epsilon}}{\partial t} = -\mathbf{U}\cdot\boldsymbol{\nabla}\overline{\epsilon} - C_{\epsilon 1}\frac{\overline{\epsilon}}{\overline{k}}\overline{\tau}_{ij}S_{ij} - C_{\epsilon 2}\frac{\overline{\epsilon}^2}{\overline{k}} + C_{\epsilon 3}\frac{\overline{\epsilon}}{\overline{k}}\frac{\nu_T}{\overline{\theta}}\frac{\partial(\overline{\theta}+\theta)}{\partial x_i}\frac{\partial(\overline{p}+p)}{\partial x_i} - \mathcal{R} + \frac{\partial}{\partial x_i}\left(\alpha_\epsilon \nu \frac{\partial \overline{\epsilon}}{\partial x_i}\right) \quad (5)$$

$$\nu = \nu_0 + \nu_T, \qquad \nu_T = C_\mu \frac{\overline{k}^2}{\overline{\epsilon}}, \quad (6)$$

where all nonbarred variables represent perturbations from the model base state. The turbulence closure method we use is the k–ϵ model of Yakhot and Orszag (1992) with the addition of a term in both the turbulent kinetic energy ($\overline{k}$) and turbulent kinetic energy dissipation ($\overline{\epsilon}$) equations representing the effect of buoyant generation and dissipation of turbulent kinetic energy (Dovgalyuk et al. 1994), which is often significant in statically unstable dynamically active regions of the model domain. Values of model constants, as well as variable nomenclature, are identical to that of Yakhot and Orszag (1992), with the exception of the constant $C_{\epsilon 3}$, which follows that of Dovgalyuk et al. (1994). The k–ϵ model is an attractive closure method because its implementation does not involve significant modifications of the model equations, and the method provides accuracy comparable to more complicated closure methods. We use a value of 20.0 m^2 s^{-1} for ν_0, 1.0 m^2 s^{-2} for $\overline{k}_0$, and 0.017 m^2 s^{-3} for $\overline{\epsilon}_0$, which leads to ν_{T0} = 5.0 m^2 s^{-1}. All model simulations were run on 144 nodes of the Wisconsin Model Engine (WME), an in-house transputer-based parallel supercomputer.

3. Methodology

As in Anderson et al. (1992), microburst forcing is initiated by a four-dimensional cooling function that parameterizes the effects of thermodynamic cooling produced by a cumulonimbus cloud. The spatial nature of the cooling function Q is identical for all runs and is specified by

$$Q(x, y, z, t) = \begin{cases} g(t)\cos^2\pi R & \text{for } R < \dfrac{1}{2} \\ 0 & \text{for } R > \dfrac{1}{2}, \end{cases} \quad (7)$$

where the temporal function $g(t)$ increases from 0 to a maximum cooling rate of -0.030 K s^{-1} over the first 2 min of model integration and decays after 12 min

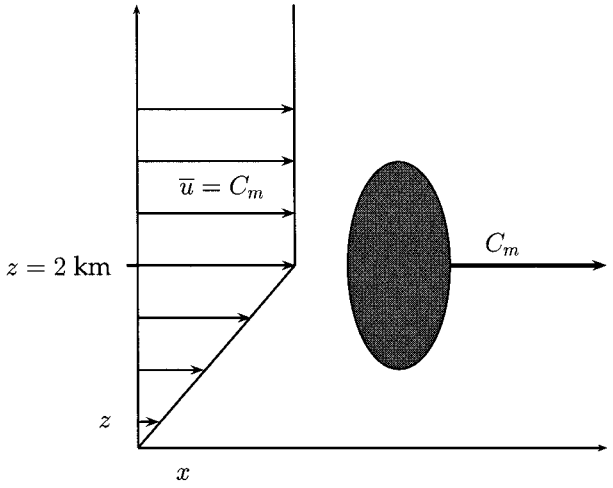

FIG. 1. The experimental design. The cooling source moves eastward at speed C_m, which is the value of the unidirectional environmental winds ($\overline{u}$) above 2 km. Environmental winds below 2 km decay linearly to 0 m s^{-1}at the surface.

model time. The scaled distance from the cooling source center is R and is determined by

$$R = \sqrt{\left(\frac{x - x_0}{h_x}\right)^2 + \left(\frac{y - y_0}{h_y}\right)^2 + \left(\frac{z - z_0}{h_z}\right)^2}, \quad (8)$$

where (x_0, y_0, z_0) is the spatial location of geometric center of the cooling function. The cooling function horizontal half-width $h_x = h_y$ = 1200 m and the vertical half-width h_z = 1800 m. The forcing function parameters were chosen to produce similar forcing found in microburst-producing thunderstorm simulations performed by Straka and Anderson (1993), who used a three-dimensional cloud model with detailed ice microphysics. The size and elevation of the cooling forcing function also agree well with the observations of Lee et al. (1992a). Similarly, Knupp (1989) observed that in both his dry and wet microburst simulations using a cloud model, downdraft initiation occurred immediately below the melting level, which is at ~2 km AGL.

Five moving-source runs are examined, as well as a static-source run for comparison. For each of the moving-source runs, the cooling forcing function moves in an eastward direction with a speed of C_m, where C_m = 3, 6, 9, 12, and 15 m s^{-1}. The environmental wind profiles for each of these runs matches the speed and direction of the cooling source 2 km and above, and linearly decays to zero at the surface (see Fig. 1). We are therefore parametrically modeling the region below a cloud that is assumed to be moving with the environmental winds and is thermodynamically forcing a microburst into the boundary layer. The unidirectional environmental winds are consistent in structure with observed sheared boundary layers in which microburst-producing storms have been observed (Lee et al. 1992a; Knupp 1996).

A primary goal of this study is to understand the relationship between source velocity and downshear surface wind velocity. The strong surface winds that form when the downdraft winds turn into the horizontal plane are one of the most tangible features of microbursts to humans. Observations of damage patterns left by microbursts often reveal strong unidirectional flow rather than the radial flow expected from a static isolated microburst. These ''straight-line winds'' are often unusually strong and have been attributed to traveling microbursts (Fujita 1985). In order to better understand the relationship between storm velocity and surface wind velocity, we examine components of the u momentum equation as well as a Lagrangian kinetic energy (K) analysis of the fastest surface winds of all runs. Because of the dominance of pressure forces on the acceleration of surface horizontal winds, we perform an analysis of the diagnostic pressure equation following Rotunno and Klemp (1982). The diagnostic pressure equation for a shallow, inviscid anelastic system is as follows:

$$\pi \sim -\nabla^2\pi = \underbrace{\left(\frac{\partial u}{\partial x}\right)^2 + \left(\frac{\partial v}{\partial y}\right)^2 + \left(\frac{\partial w}{\partial z}\right)^2}_{\pi_{\text{div}}} + \underbrace{2\left(\frac{\partial u}{\partial y}\frac{\partial v}{\partial x} + \frac{\partial u}{\partial z}\frac{\partial w}{\partial x} + \frac{\partial v}{\partial z}\frac{\partial w}{\partial y}\right)}_{\pi_{\text{rot}}} \underbrace{- g\frac{\partial}{\partial z}\left(\frac{\theta}{\overline{\theta}}\right)}_{\pi_{\text{buoy}}}, \tag{9}$$

where π is the nondimensional pressure. Because we are interested in contributions toward π of each of the three forcing mechanisms (divergence, rotation/deformation, and buoyancy), we solve a Poisson equation using Jacobi relaxation for each of the individual forcing terms. These equations are solved in x–z slices through the center of the microburst downdraft, which includes the region of strongest u surface winds. We then examine $\partial\pi_{\text{div}}/\partial x$, $\partial\pi_{\text{rot}}/\partial x$, $\partial\pi_{\text{buoy}}/\partial x$, and the sum of these terms, $\partial\pi_{\text{tot}}/\partial x$. The fact that our model is quasi-compressible and not steady state means that the above formulation for π is not exact; however, a comparison of $(1/\rho)\partial p/\partial x$ using model diagnostic variables and $\partial\pi_{\text{tot}}/\partial x$ for each of these runs reveals that the error incurred by assuming incompressibility are of second-order importance.

We also examine the mechanisms behind the generation of elevated horizontal vorticity, as in Lee et al. (1992b). The kinetic energy (K) and vertical vorticity (ζ) equations, accounting for our prescribed $\overline{u}(z)$ and neglecting of the earth's rotation and turbulence, are as follows:

$$\frac{\partial K}{\partial t} = \underbrace{-\left[(u + \overline{u})\frac{\partial K}{\partial x} + v\frac{\partial K}{\partial y}\right] - w\frac{\partial K}{\partial z}}_{\text{advection}} \underbrace{- \frac{1}{\overline{\rho}}\mathbf{V}\cdot\nabla p}_{\text{pressure}} \underbrace{+ gw\frac{\theta}{\overline{\theta}}}_{\text{buoyancy}} \tag{10}$$

$$\frac{\partial \zeta}{\partial t} = \underbrace{-\left[(u + \overline{u})\frac{\partial \zeta}{\partial x} + v\frac{\partial \zeta}{\partial y}\right] - w\frac{\partial \zeta}{\partial z}}_{\text{advection}} \underbrace{- \zeta\nabla_H\cdot\mathbf{V}_H}_{\substack{\text{horizontal}\\ \text{divergence}}} \underbrace{+ \left(\frac{\partial w}{\partial y}\frac{\partial(u + \overline{u})}{\partial z} - \frac{\partial w}{\partial x}\frac{\partial v}{\partial z}\right)}_{\text{tilting}}, \tag{11}$$

where $K = \frac{1}{2}|\mathbf{V}|^2$ and $\zeta = \partial v/\partial x - \partial u/\partial y$, and all nonbarred prognostics (u, v, w, θ, and p) are perturbations from the base state. The terms in the K equation are the horizontal and vertical advection, pressure work, and buoyancy terms. The ζ equation terms are horizontal and vertical advection, horizontal divergence, and tilting terms. The horizontal divergence term can be closely approximated as $+\zeta\partial w/\partial z$ observing continuity and disregarding the contribution of sound waves.

The tilting term in (11) can be written as

$$\eta\frac{\partial w}{\partial y} + \xi\frac{\partial w}{\partial x}, \tag{12}$$

where $\xi = \partial w/\partial y - \partial v/\partial z$ and $\eta = \partial(u + \overline{u})/\partial z - \partial w/\partial x$ are the x and y components of vorticity.

Our general philosophy for these types of fluid dynamics studies is to make the experiment as simple as possible without sacrificing consistency and to make the experiments easily reproducible by other members of the scientific community. The cooling function and en-

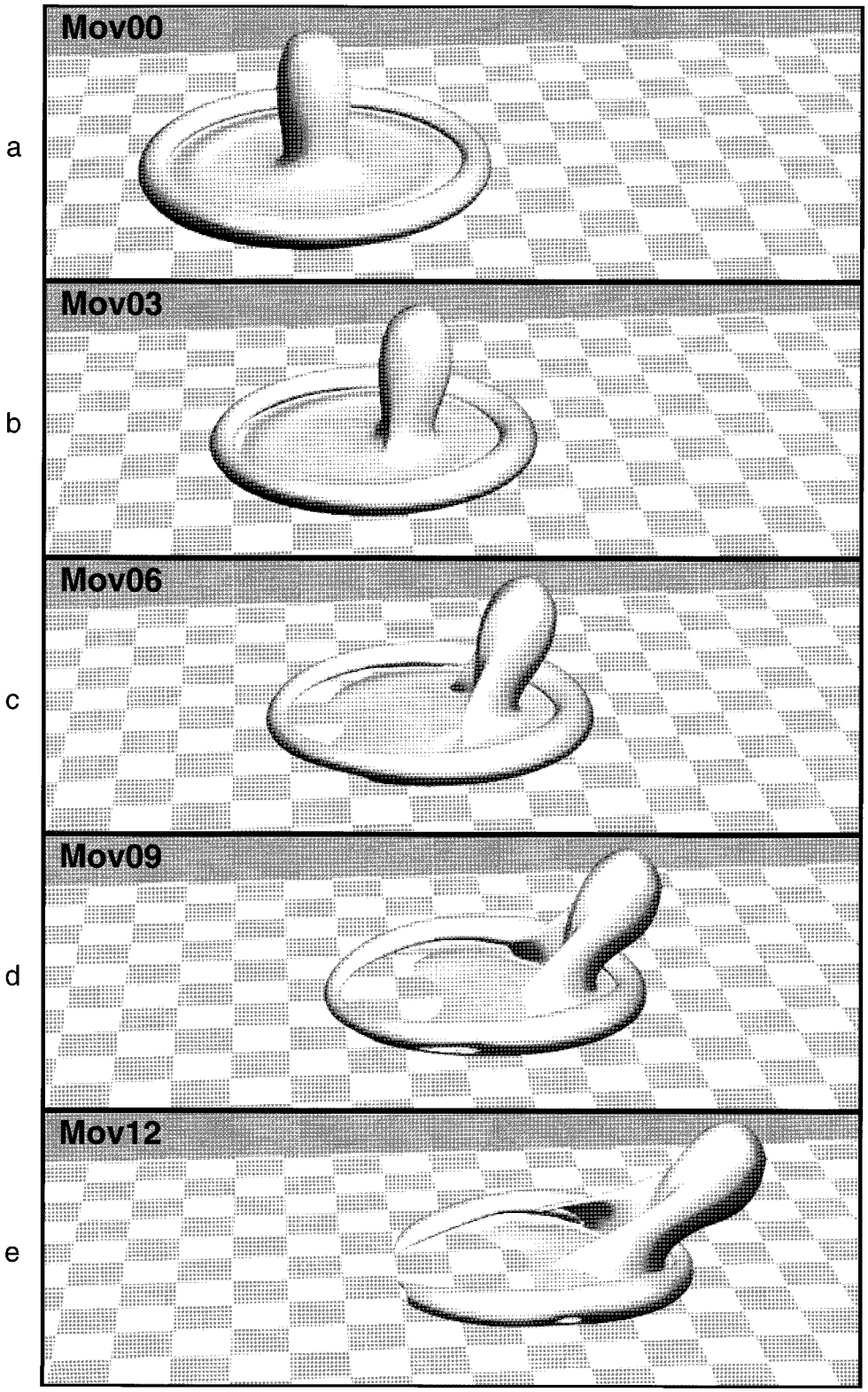

FIG. 2. The −1.5 K isosurface of θ for (a) Mov00 (static source), (b) Mov03, (c) Mov06, (d) Mov09, and (e) Mov12 model runs at 11 min model time. The cooling forcing for all runs originates at the same spatial location in the model domain. Grid squares are 1 × 1 km.

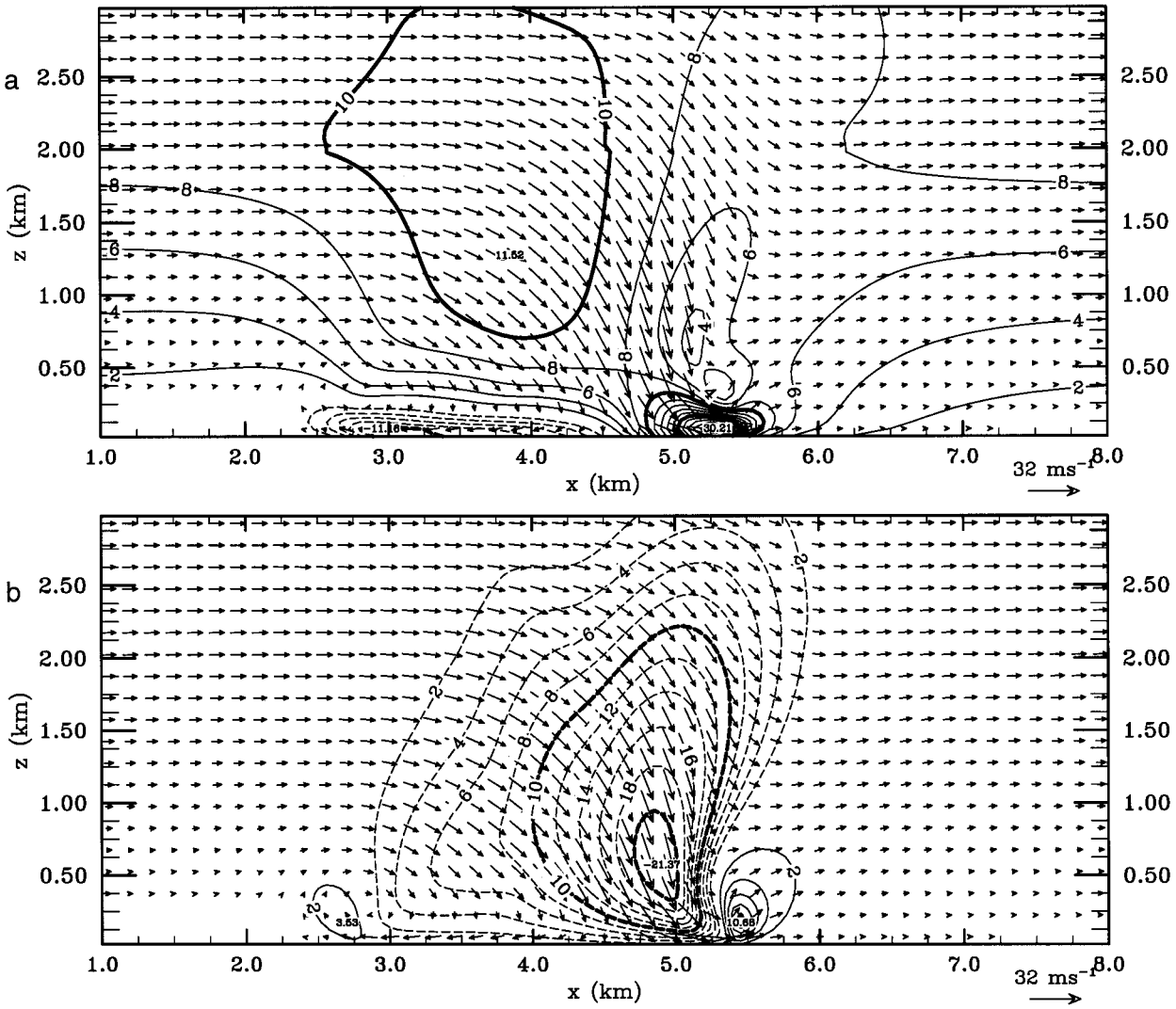

FIG. 3. An *x*–*z* plot of (a) *u*, and (b) *w* (in m s^{-1}) through the center of the microburst shortly after the downdraft of Mov09 impinges the surface. Near-surface horizontal winds exceeding 30 m s^{-1} are found at this time. Ground-relative wind vectors are plotted every third grid point.

vironmental wind profiles are idealized yet consistent with observations of some microburst phenomena. By using these simplifications, we are able to focus on the dynamics of the subcloud environment with detail that is not feasible with a full cloud model using today's technology. As such, this study should be viewed as a complement to studies that use full cloud models to explore the morphologies of microburst-producing storms.

4. Results

a. Physical characteristics

Our naming convention for all runs is Mov*xx*, where *xx* is C_m, the source velocity and environmental *u* winds above the shear layer. Figure 2 shows the −1.5 K isosurface of the potential temperature perturbation θ for Mov00, Mov03, Mov06, Mov09, and Mov12 runs at 12 min model time. Because the subcloud environment is neutrally stratified and the only source of diabatic cooling is the prescribed cooling forcing, potential temperature can be viewed as a tracer and can be used to examine the physical characteristics of the wind flow. As C_m is increased, the microburst downdraft core is displaced eastward relative to the geometric center of the microburst outflow for the static-source case. Surface outflow velocity in the shear normal direction decreases with increasing C_m, while the velocity of the outflow in the direction of source movement increases. The increase in downshear outflow head velocity is correlated with stronger horizontal velocities in the direction of source movement. An *x*–*z* plot of *u* winds on

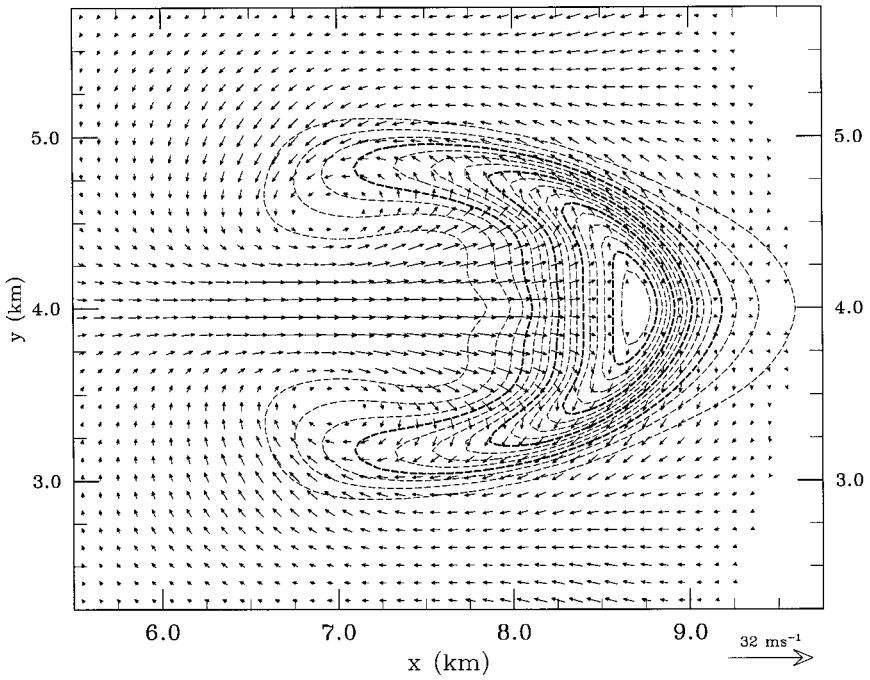

FIG. 4. The x–y slice of θ for Mov09, 1 km AGL at 15 min model time. Thin contours are drawn every $-\frac{1}{3}$ K, thick contours every -1 K. Vectors represent perturbation horizontal winds and are plotted every other grid point.

the mirror axis (through the center of the downdraft) for Mov09 (see Fig. 3a) shows horizontal velocities exceeding 30 m s^{-1} shortly after the downdraft impinges the surface. Stronger u winds above 500 m AGL trailing the moving downdraft core are caused by the vertical advection of elevated horizontal winds by the downdraft, which can also be seen in the shape of the θ isosurfaces in Fig. 2. The downdraft remains erect in the presence of shear while the downshear horizontal gradient of w is increased, which is a key factor in the evolution of surface horizontal winds (see Fig. 3b). Rotunno and Klemp (1982) observed a similar response to shear by vertical circulations in their examination of updraft structure in the presence of unidirectional shear. Evidence of significant vertical vorticity can be be seen in Fig. 4 and also in the shape of the lagging cold downdraft air that flanks the downdraft core in the moving-source runs depicted in Fig. 2. As C_m increases, the momentum of westward-flowing near-surface winds is weakened, as well as the magnitude of θ, due to a smaller mass flux in the upshear propagating outflow. This asymmetry in the surface outflow is especially apparent in the faster traveling microburst simulations.

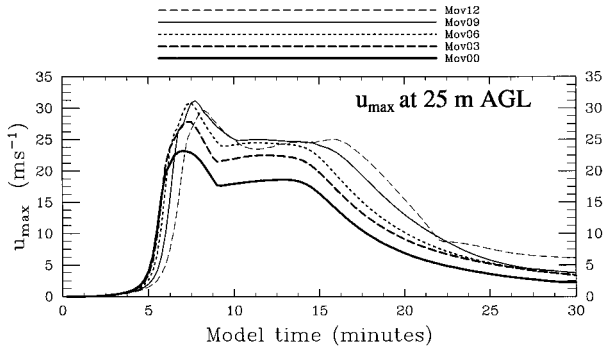

FIG. 5. A time series of maximum values of the u component of the horizontal wind at 25 m AGL for Mov00, Mov03, Mov06, Mov09, and Mov12.

b. *The* u *momentum and kinetic energy budgets*

Figure 5 is a time series plot of the strongest horizontal winds (u_{max}) found 25 m AGL for Mov00–Mov12. In all moving-source cases, u_{max} is the positive eastward component of u and is found along the center of the microburst outflow to the east of the downdraft core (see Fig. 6). These winds are found in the wall jet[1] region of the microburst outflow, which occurs immediately above the surface friction layer. These runs exhibit an initial outflow peak velocity, followed by a leveling-off period where u_{max} is relatively constant until the cooling forcing is turned off. In order to understand

[1] The term ''wall jet'' is used in fluid dynamics to describe the type of shallow flow that occurs when a fluid impinges on a plane surface at high velocity. Proctor (1988) first used this term to describe the analogous horizontal outflow that occurs with microbursts, and we follow this nomenclature.

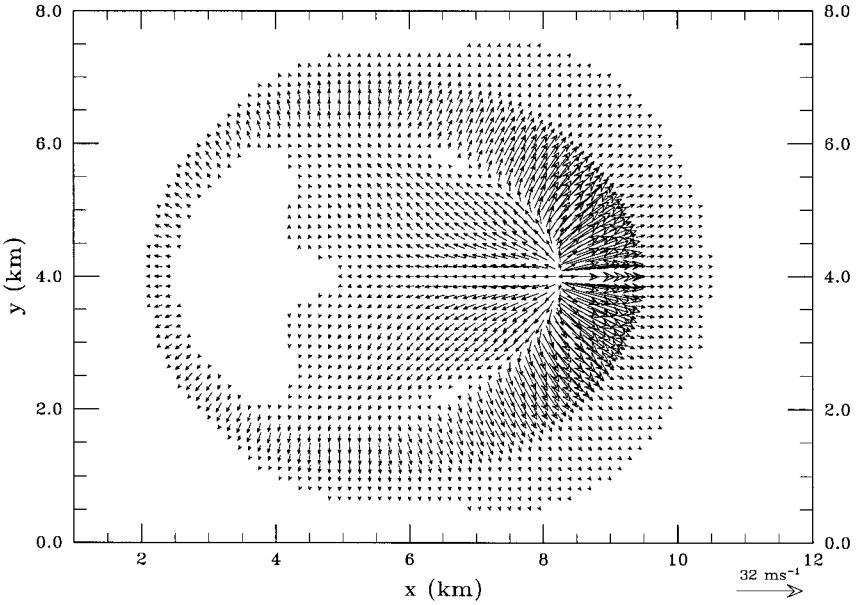

FIG. 6. Horizontal wind vectors 25 m AGL for Mov09 at 12 min model time, plotted every other grid point. Eastward-traveling winds exceeding 30 m s^{-1} are found at this height.

the surface horizontal winds, it is illustrious to first observe the morphology of the microburst downdraft. The rapidly cooling, negatively buoyant air initially builds up as gravity works to accelerate it downward. This leads to an initial surge of cold downdraft air, which initiates strong vertical convergence [large values of $(\partial w/\partial z)^2$] forcing a high-pressure ''dome,'' which acts to turn the downward winds into the horizontal plane. Before the downdraft winds impinge the surface, a baroclinically generated rotating ring of air, or roll vortex, forms around the descending downdraft. The downdraft impinges the surface and diverges outward, forming the shallow horizontal wall jet, which spreads radially outward behind the roll vortex.

As is evident from Fig. 5, the relationship between C_m and $u_{\max}$ is not linear. The difference in peak $u_{\max}$ between Mov00 and Mov03 is 4.6 m s^{-1}, while the difference for Mov06 and Mov09 is only 0.4 m s^{-1}. In

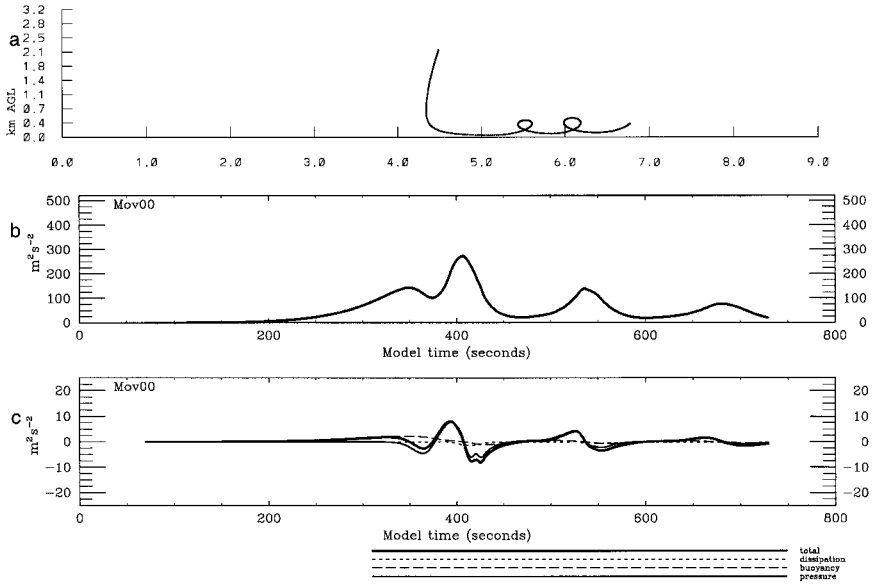

FIG. 7. Characteristics of a trajectory that passes through the strongest surface horizontal winds for Mov00; (a) trajectory path, (b) kinetic energy, and (c) kinetic energy forcing terms along the trajectory path.

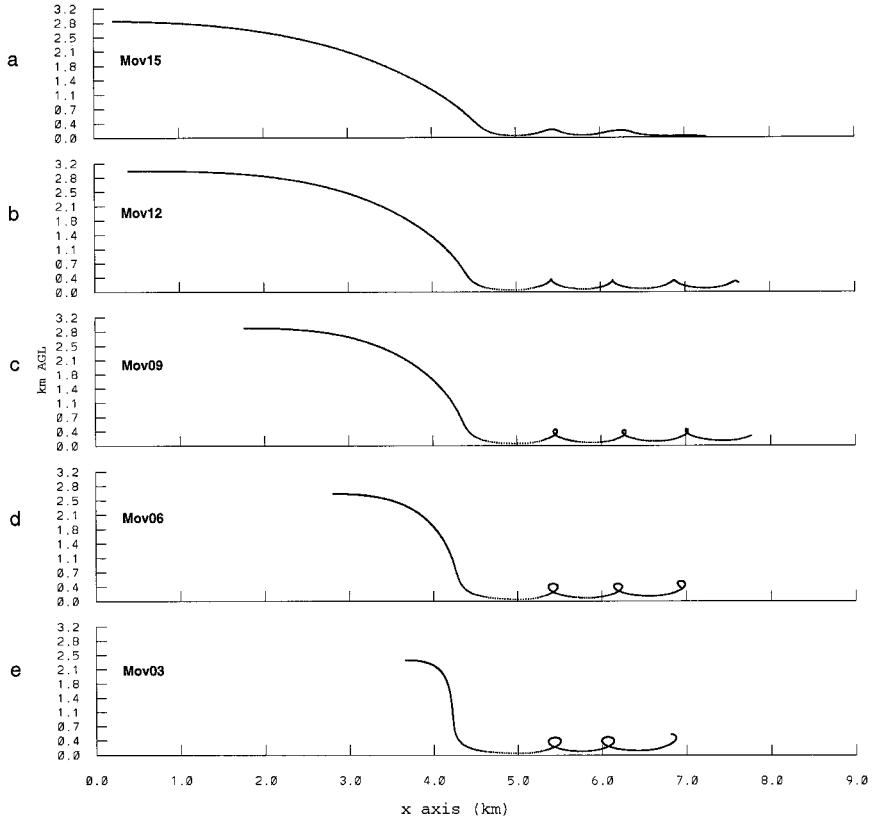

FIG. 8. Paths of trajectories that travel through the strongest surface winds for (a) Mov15, (b) Mov12, (c) Mov09, (d) Mov06, and (e) Mov03. The origin of the Mov15 trajectory is farther west than depicted above.

the case of Mov12, peak $u_{\max}$ is actually less than that of Mov09, and the profile of $u_{\max}$ for Mov12 does not exhibit the same steady flow characteristics of the other runs. In order to better understand the relationship between C_m and $u_{\max}$ a Lagrangian analysis of kinetic energy forcing [(10)] is conducted by following a trajectory that passes through the strongest surface winds of each run. The trajectory path is calculated by using model data every 5 s and using a linearly interpolated trajectory time step of 1 s. The trajectory genesis point for all of the runs is located directly east of the downdraft core, directly above the surface friction layer, and occurs shortly after the downdraft impinges the surface. The trajectory is integrated backward and forward in time from the genesis point, and values along the trajectory are calculated using a spatial cubic spline interpolant weighed linearly in time between the two adjacent model time levels. We first investigate the Mov00 run. Figure 7 contains plots of the trajectory and the values of kinetic energy and kinetic energy forcing along the trajectory path. Because the strongest u winds are found on the mirror axis where there is no v component of the wind, the parcels remain in the x–z plane and may be examined in two dimensions. The Mov00 parcel originates a height of about 2 km, which is the vertical center of maximum cooling forcing. This parcel travels down the eastern flank of the downdraft core where it is accelerated by the negatively buoyant colder air. The parcel decelerates as it enters the surface pressure dome and is turned into the horizontal plane and ejected eastward where it receives its maximum velocity. The parcel then gets advected into the roll vortex circulation where it remains for the remainder of the simulation. The kinetic energy forcing shows that while buoyant forces provide all of the descending parcel's kinetic energy, pressure forces dominate in how this kinetic energy is redistributed. Diffusion kinetic energy is strongest near the surface and serves only as an energy sink, and is of second-order importance for the purpose of this comparative study.

The equivalent trajectory for the moving-source runs show a similar forcing regime to the Mov00 run, although there are important differences. Trajectory paths that pass through the strongest u winds for the moving source runs are are shown in Fig. 8. Parcel kinetic energy along each path is shown in Fig. 9 and the kinetic energy forces acting on these parcels are depicted in Fig. 10. As the source speed is increased, the descending trajectory receives less deceleration as it approaches the ground. Figure 11 suggests that this is is due to the fact

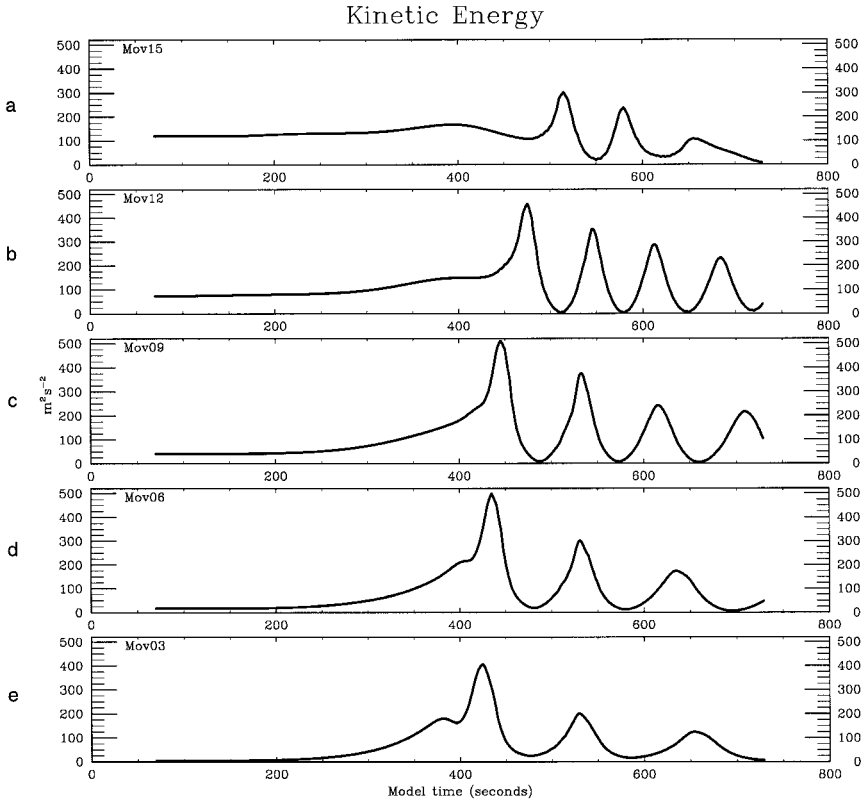

FIG. 9. Values of kinetic energy along the trajectory paths depicted in Fig. 8: (a) Mov15, (b) Mov12, (c) Mov09, (d) Mov06, and (e) Mov03.

that pressure kinetic forcing [see Eq. (10)] in the region of the pressure dome is decreased with increasing source speed. The larger values of pressure kinetic energy forcing to the east of the pressure dome for the moving-source runs are correlated with the larger values of u (this is investigated further below). The periodic acceleration/deceleration pattern seen following the initial kinetic energy peak occurs as the parcel ascends out of and descends into the wall jet as it travels within the roughly cyclostrophically balanced roll vortex circulation. The shorter period of this oscillation as the source speed increases is due to an increasingly smaller roll vortex radius at the leading edge of the outflow (this behavior bears further investigation).

As the source speed exceeds 12 m s^{-1}, the peak outflow velocity begins to decrease. This decrease is correlated with a decrease in buoyancy forcing due to the structure of the cooling function. Because the lower half of the cooling forcing function (which has units of K s^{-1}) is moving faster than the environmental winds, air below the shear level for the moving-source runs receives less cooling and therefore less total buoyancy forcing. This decrease in buoyancy is reflected by smaller peak downdraft values (see Fig. 12), which are especially pronounced for Mov12 and Mov15. Despite the decrease in downdraft speed, all moving source runs exhibit stronger surface pressure forcing than Mov00, leading to larger peak surface u winds.

An examination of the solution to the diagnostic pressure equation [(9)] reveals that rotational forces make the strongest contribution toward the magnitude of the pressure field in the region of strongest horizontal winds. Nearly all of the variation in the structure of the pressure field is also represented by the rotational term, which is $2(\partial u/\partial z)/(\partial w/\partial x)$ on the mirror axis. Values of the contribution toward the pressure field by the divergence and buoyancy terms (not shown) are of significantly smaller magnitude than the rotational term, and variations in these terms between runs are also comparatively much smaller. Figure 13 depicts values of $\partial \pi_{\text{rot}}/\partial x$ pressure forcing as calculated from solving the diagnostic pressure equation. In the downshear portion of the downdraft, $\partial \pi_{\text{rot}}/\partial x$ increases substantially as C_m increases from 0 to 9 m s^{-1}. An examination of the w field in this region suggests that the increase in magnitude of this term is due to larger values of $\partial w/\partial x$ with increasing C_m (see Fig. 3b). The strongest values of u are found to the east of this region, slightly upshear of the center of the roll vortex circulation where additional acceleration is imposed by the cyclostrophically induced pressure gradient. The correlation between $\partial \pi_{\text{rot}}/\partial x$ and peak u winds is also seen in Mov15, where a decrease

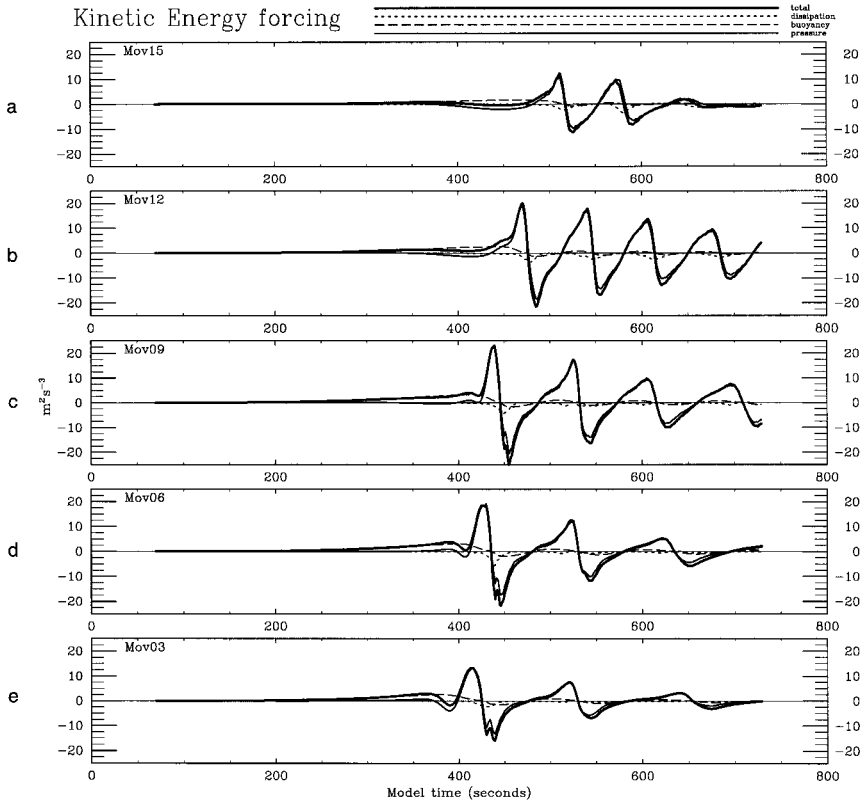

FIG. 10. Values of kinetic energy forcing along the trajectory paths depicted in Fig. 8: (a) Mov03, (b) Mov06, (c) Mov09, (d) Mov12, and (e) Mov15.

in both terms is found. The ability of the roll vortex circulation to contribute toward strong surface horizontal winds due to pressure forcing is suggested by the following two observations.

1) Increases in u_{max} with increasing source speed are directly correlated with stronger pressure kinetic energy forcing directly upshear of the center of the roll vortex (see Fig. 11).
2) Nearly all of the contribution to the pressure forcing is due to the rotational term in (9).

However, the unusually strong peak horizontal winds are short lived and occur only while the roll vortex is adjacent to the dynamically forced surface pressure dome. This suggests that it is the combined pressure forcing of both features in this particular geometry that is responsible for the peak values of u_{max} observed in Fig. 5. The ability of roll vortices to contribute toward accelerating horizontal winds was also observed in Orf et al. (1996), where unusually strong elevated jet circulations were found to occur adjacent to elevated roll vortices in certain cases of colliding microburst outflows.

c. Vertical vorticity

Rotunno and Klemp (1982) demonstrated that an updraft in a unidirectionally sheared environment will impose rotation about a vertical axis due to the tilting of environmental vorticity. A downdraft in a similar environment would therefore be expected to exhibit similar behavior, which would be reflected in the vertical vorticity field. An example of this can be seen in the vorticity parameters of Mov12 in Fig. 14, which is a horizontal cross section located at 1225 m AGL for Mov12 at 7 min model time. Largest values of ζ for the traveling microburst simulations are consistently found near this height. As the downdraft winds form at this level, a region of strong positive ξ vorticity is initially generated north of the downdraft core due to the $\partial w/\partial y$ component of the tilting term in (11). Because the cooling source is moving in a sheared environment, the downdraft is asymmetric and the region of strongest ξ is found where there is a strong positive $\partial w/\partial x$ component. Hence, from (12) it is evident that this region is one where ζ vorticity will grow by tilting of ξ vorticity. Growth of ζ due to stretching becomes stronger later in the run where there is an overlap between the spreading vertical circulation and vertical variation in the strength of the downdraft. Our results suggest that local regions of significant horizontal vorticity can be generated by a typical High Plains cumulonimbus cloud occurring in a unidirectionally sheared environment. These numerical results are in agreement with the observations and conceptual model of Lee et al. (1992b),

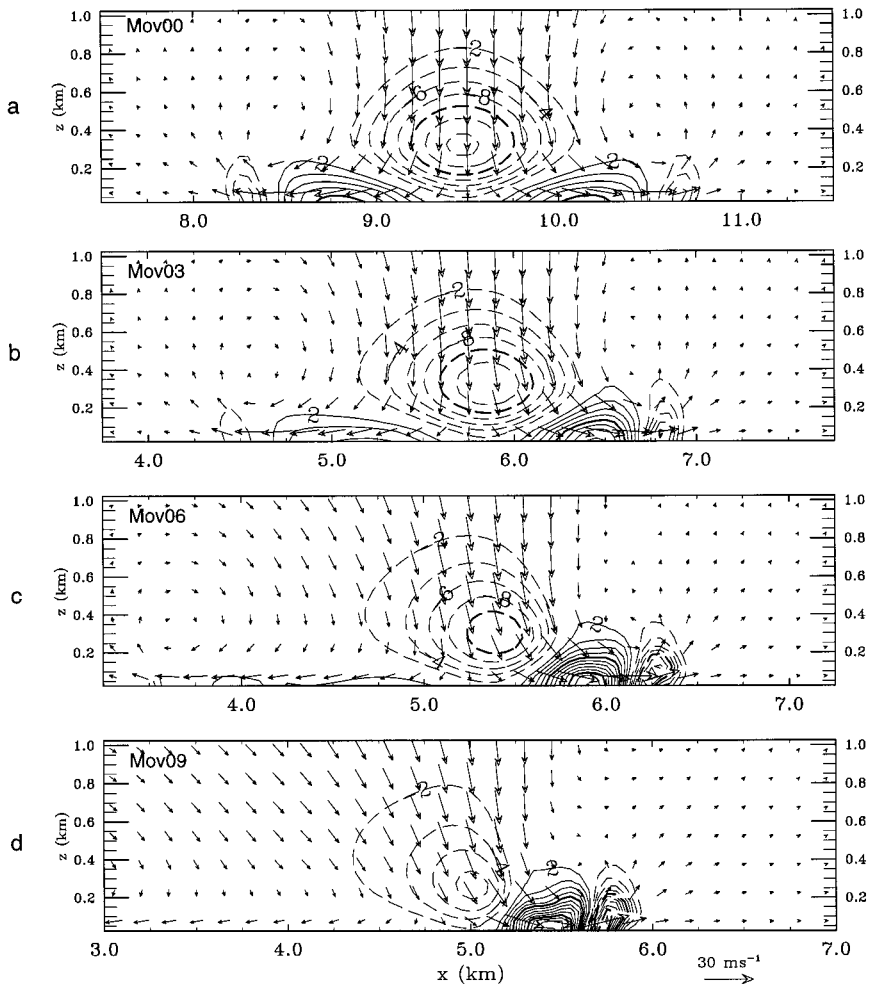

FIG. 11. An x–z plot of pressure kinetic energy forcing $[-(1/\rho)\mathbf{V}\cdot\nabla p]$ through the center of the microburst downdrafts for (a) Mov00, (b) Mov03, (c) Mov06, and (d) Mov09. Thin contours are plotted every 2 $m^2\ s^{-3}$ and thick contours are plotted every 10 $m^2\ s^{-3}$. Arrows represent x–z wind vectors with $\bar{u}(z)$ removed and are plotted every third grid point.

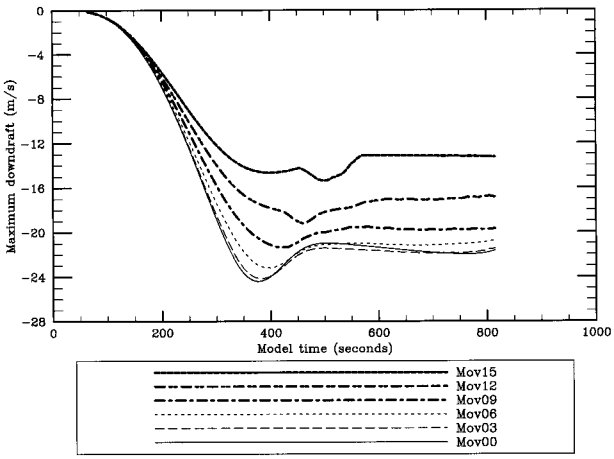

FIG. 12. Values of the peak downdraft speed as a function of time for all runs.

who attribute a vorticity couplet to the formation of an observed bow echo in a nonsupercell microburst-producing thunderstorm that occurred in an environment with a similar shear profile to that of our moving-source experiments.

5. Summary

Five three-dimensional numerical simulations of moving-source microbursts were performed in unidirectionally sheared subcloud environments, and kinetic energy and horizontal momentum budgets of each simulation were examined and compared to that of an isolated microburst occurring in a quiescent environment. We find that an increase in the source speed from 0 to 9 m s^{-1} is matched with an increase in the strength of the outflow in the direction of source movement. While the experimental design dictates that all of the initial kinetic energy of the simulations is due to the buoyancy

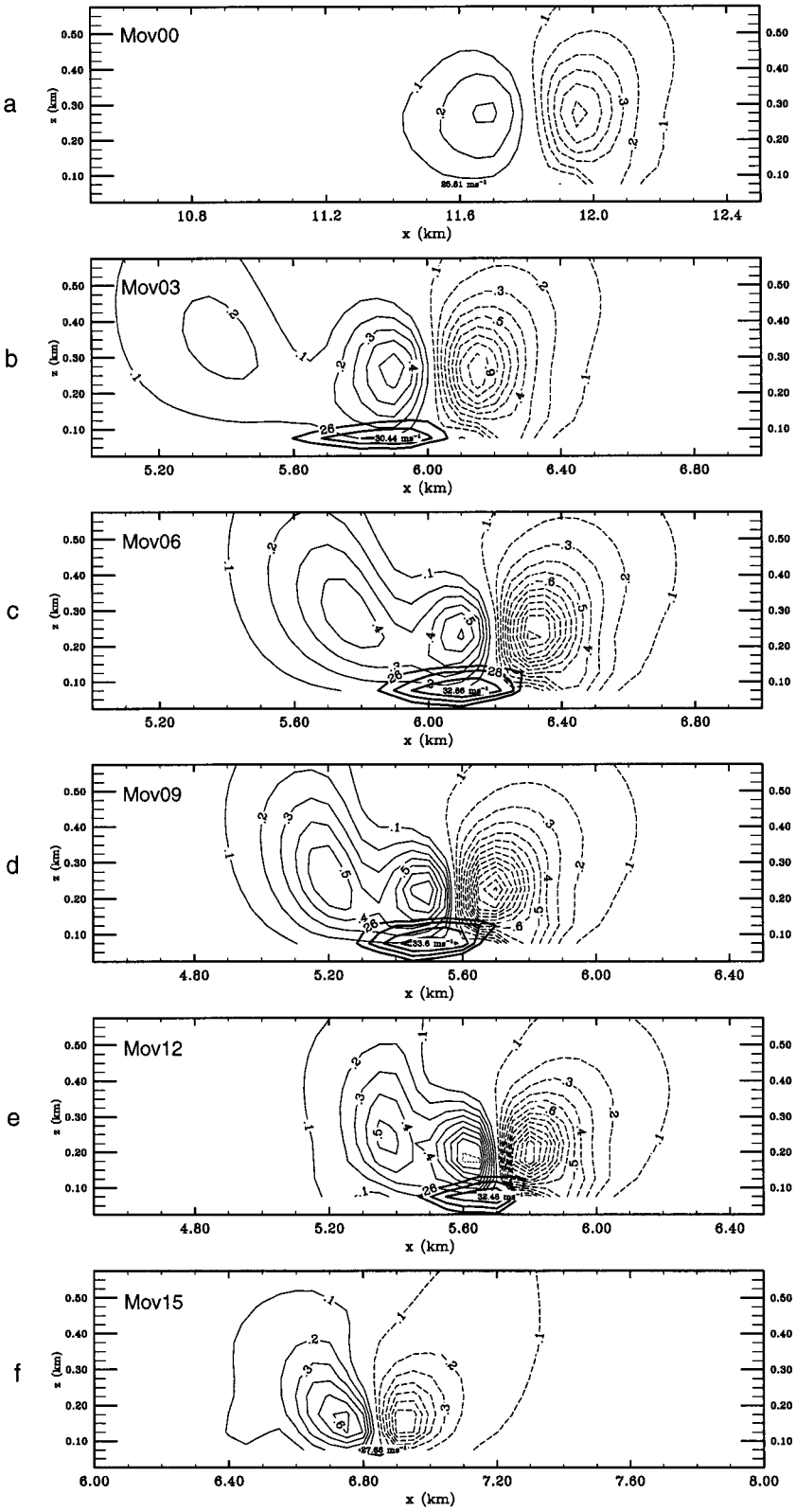

FIG. 13. Values of the acceleration due to rotational pressure forces on the u wind, or $\partial\pi_{\text{rot}}/\partial x$, for (a) Mov00, (b) Mov03, (c) Mov06, (d) Mov09, (e) Mov12, and (f) Mov15 during the period of strongest horizontal velocity. Here, $\partial\pi_{\text{rot}}/\partial x$ is contoured every 0.1 m s^{-2}, and thick lines represent values of u exceeding 25 m s^{-1} in 2 m s^{-1} intervals.

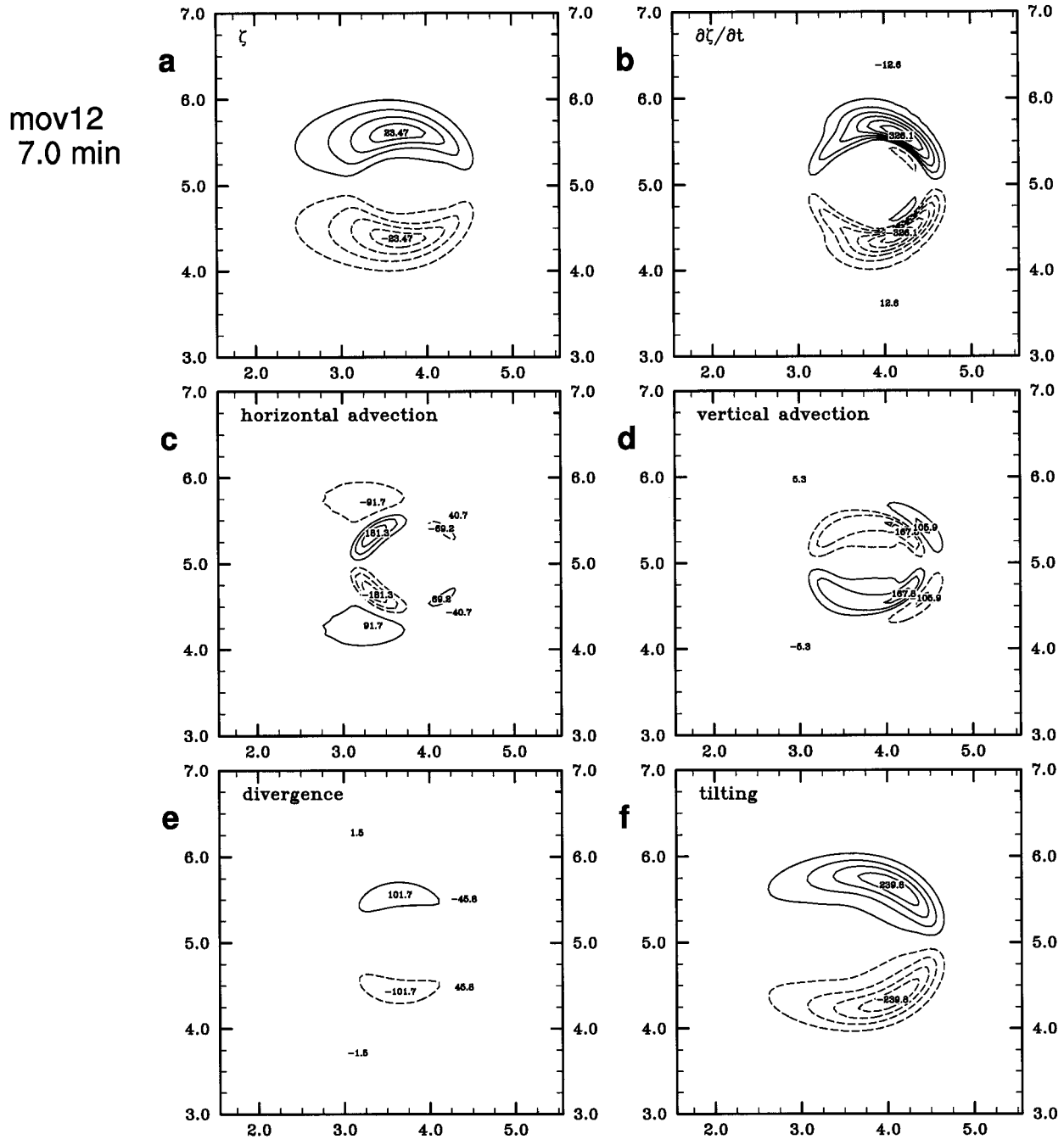

FIG. 14. The *x–y* slices of (a) ζ, (b) $\partial\zeta/\partial t$, (c) horizontal advection of ζ, (d) vertical advection of ζ, (e) divergence of ζ, and (f) tilting of ζ. All plots are of the Mov12 run at 1225 m AGL at 7 min model time. Contours of ζ are drawn every 5×10^{-3} s^{-1}, and contours of the source terms are drawn every 50×10^{-6} s^{-2}. Units for ζ are 10^{-3} s^{-1} and are 10^{-6} s^{-2} for the source terms.

forcing of the cooling source, it is the redistribution of this kinetic energy by pressure forces that cause the major variations in the wall jet winds in the direction of the cooling source. A decomposition of the diagnostic pressure equation shows that this behavior is dominated by rotational pressure forces imposed by locally strong horizontal variations in the magnitude of the downdraft and the presence of an adjacent surface roll vortex. The increase of peak horizontal winds with increasing shear/source movement occurs despite a decrease in the total buoyancy imposed by the moving cooling source in the faster moving runs. These results support observations that low-level vertical shear can have a significant impact on the dynamics of microburst outflows, and sug-

gest that a typical microburst-producing High Plains cumulonimbus cloud can produce significantly stronger horizontal winds on the ground by virtue of movement in a unidirectionally sheared environment. The asymmetric outflow patterns produced by these simulations match microburst outflows in similar environments that have been observed in the High Plains of the United States.

As has been observed in other studies of vertical perturbations in a sheared environment, regions of locally strong horizontal vorticity are generated by the tilting of environmental vorticity by the downdraft. These regions of vorticity, which are enhanced by vortex stretching, flank the downdraft in the form of a vorticity couplet, which is similar in structure to an observed case of a bow-echo microburst that occurred in an environment similar to those of our our idealized simulations.

Acknowledgments. The University of Wisconsin—Madison WME project was made possible by the generous support of the UW Graduate School. Parts of this work have been funded by the Federal Aviation Administration. The authors would like to thank the reviewers for contributing many useful observations and critiques in helping finalize this paper. Isosurface renderings were produced by POV-Ray and line drawings were produced by NCAR Graphics. The U.S. government assumes no responsibility for this work or the use thereof.

REFERENCES

Alahyari, A., and E. K. Longmire, 1995: Dynamics of experimentally simulated microbursts. *AIAA J.*, **33,** 2128–2136.

Anderson, J. R., L. G. Orf, and J. M. Straka, 1992: A 3-D model system for simulating thunderstorm microburst outflows. *Meteor. Atmos. Phys.*, **49,** 125–131.

Dovgalyuk, Y. A., M. A. Zatevakhin, and E. N. Stankova, 1994: Numerical simulation of a buoyant thermal using the k–ϵ turbulence model. *J. Appl. Meteor.*, **33,** 1118–1126.

Fujita, T. T., 1979: Objectives, operation, and results of project NIMROD. Preprints, *11th Conf. on Severe Local Storms,* Kansas City, MO, Amer. Meteor. Soc., 259–266.

——, 1985: *The Downburst: Microburst and Macroburst.* The University of Chicago Press, 122 pp.

Hjelmfelt, M. R., 1988: Structure and life cycle of microburst outflows observed in Colorado. *J. Appl. Meteor.,* **27,** 900–927.

——, H. D. Orville, R. D. Roberts, J. P. Chen, and F. J. Kopp, 1989: Observational and numerical study of a microburst line-producing storm. *J. Atmos. Sci.,* **46,** 2731–2743.

Knupp, K. R., 1989: Numerical simulation of low-level downdraft initiation within precipitating cumulonimbi: Some preliminary results. *Mon. Wea. Rev.,* **117,** 1517–1529.

——, 1996: Structure and evolution of a long-lived, microburst-producing storm. *Mon. Wea. Rev.,* **124,** 2785–2806.

Lee, W.-C., R. E. Carbone, and R. M. Wakimoto, 1992a: The evolution and structure of a ''bow-echo–microburst'' event. Part I: The microburst. *Mon. Wea. Rev.,* **120,** 2188–2210.

——, ——, and ——, 1992b: The evolution and structure of a ''bow-echo–microburst'' event. Part II: The bow echo. *Mon. Wea. Rev.,* **120,** 2211–2225.

Lin, Y.-J., and R. G. Hughes, 1987: Structural features of a microburst-producing storm in Colorado revealed by JAWS dual-Doppler radars. *J. Atmos. Sci.,* **44,** 3640–3655.

——, and J. A. Coover, 1988: A kinetic energy analysis of a microburst-producing thunderstorm based on JAWS dual-Doppler data. *J. Atmos. Sci.,* **45,** 2764–2771.

McCarthy, J., J. W. Wilson, and T. T. Fujita, 1982: The Joint Airport Weather Studies Project. *Bull. Amer. Meteor. Soc.,* **63,** 15–22.

Orf, L. G., J. R. Anderson, and J. M. Straka, 1996: A three-dimensional numerical analysis of colliding microburst outflow dynamics. *J. Atmos. Sci.,* **53,** 2490–2511.

Parsons, D. B., and M. L. Weisman, 1993: A numerical study of a rotating downburst. *J. Atmos. Sci.,* **50,** 2369–2385.

Proctor, F. H., 1988: Numerical simulations of an isolated microburst. Part I: Dynamics and structure. *J. Atmos. Sci.,* **45,** 3137–3160.

——, 1989: Numerical simulations of an isolated microburst. Part II: Sensitivity experiments. *J. Atmos. Sci.,* **46,** 2143–2165.

——, and R. L. Bowles, 1992: Three-dimensional simulation of the Denver 11 July 1988 microburst-producing storm. *Meteor. Atmos. Phys.,* **49,** 107–124.

Rotunno, R., and J. B. Klemp, 1982: The influence of shear-induced pressure gradient on thunderstorm motion. *Mon. Wea. Rev.,* **110,** 136–151.

Srivastava, R. C., 1985: A simple model of evaporatively driven downdraft: Application to microburst downdraft. *J. Atmos. Sci.,* **42,** 1004–1023.

Straka, J. M., and J. R. Anderson, 1993: Numerical simulations of microburst producing storms: Some results from storms observed during COHMEX. *J. Atmos. Sci.,* **50,** 1329–1348.

——, R. B. Wilhelmson, L. J. Wicker, J. R. Anderson, and K. K. Droegemeier, 1993: Numerical solutions of a non-linear density current: A benchmark solution and comparisons. *Int. J. Num. Methods Fluids,* **17,** 1–22.

Teske, M. E., and W. S. Lewellen, 1977: Turbulent transport model of a thunderstorm gust front. Preprints, *Tenth Conf. on Severe Local Storns,* Omaha, NE, Amer. Meteor. Soc., 143–150.

Tuttle, J. D., V. N. Bringi, H. D. Orville, and F. J. Kopp, 1989: Multiparametér radar study of a microburst: Comparison with model results. *J. Atmos. Sci.,* **46,** 601–620.

Wakimoto, R. M., 1985: Forecasting dry microburst activity over the high plains. *Mon. Wea. Rev.,* **113,** 1131–1143.

——, C. J. Kessinger, and D. E. Kingsmill, 1994: Kinematic, thermodynamic, and visual structure of low-reflectivity microbursts. *Mon. Wea. Rev.,* **122,** 72–92.

Wolfson, M. M., J. T. DiStefano, and T. T. Fujita, 1985: Low-altitude wind shear characteristics in the Memphis, TN area. Preprints, *14th Conf. on Severe Local Storms,* Indianapolis, IN, Amer. Meteor. Soc., 322–327.

Yakhot, V., and S. A. Orszag, 1992: Development of turbulence models for shear flows by a double expansion technique. *Phys. Fluids,* **4A,** 1510–1520.